Dynamic Model Inversion of a Soft Robot using Servo Constraints

Malte Grube[1], Sean Maroofi[1,2], and Robert Seifried[1]

***Abstract*— Soft robots provide various application benefits in comparison to their rigid counterparts, such as body flexibility and sensitive manipulation. For dynamic control, models must consider elastic deformation, underactuation, and redundancy. However, analytical inversion of forward dynamics is not possible due to the complexity of the model.**

We propose differentiation of a kinematic model and combination of the servo-constraints approach for underactuated multi-body system control to obtain a full dynamic model of a soft robot. We analyze the system for internal stability and apply the model to a custom real-world soft robot. Our experiments demonstrate the effectiveness of our approach in tracking dynamic trajectories, averaging a positional error of [?NUM].

I. Introduction

Soft robotics is a growing subfield of robotics research with their flexible nature offering a wide range of advantages and applications, including sensitive grasping and less constrained motion in contrast to their rigid counterparts [1]. However, their deformable nature comes at the cost of an infinite number of degrees of freedom and the need for new modeling and control schemes.

In literature, a distinction is made between quasi-static models and controllers, which neglect dynamics, and dynamic models and controllers. However, the terms quasi-static and kinematic are often used interchangeably. Most of the existing control algorithms for soft robots are based on purely quasi-static modeling [2], [3]. [? add some examples as references]. These models allow simple and accurate control as long as the motions are slow enough that the dynamics can be neglected. However, new soft robotics applications require increasingly faster and more precise motions. Therefore, dynamic models and controllers are needed and are currently being developed for soft robots.

Real-time dynamic control remains challenging due to the infinite dimensionality in the robot's state space [4]. Differentiation of deeply-nested time-dependent variables in the kinematics result in highly complex equations, which are computationally expensive to solve in real-time [5], [2]. Moreover, feedback control requires sensor integration into the soft robot, which is difficult to implement as sensors must withstand the typically high strains without destroying the softness of the robot. To overcome this, external camera tracking systems are commonly installed, but the need for a continuous clear view of the robot limits application generality across different environments. Feedforward control alone, or a combination with simple feedback control, can dramatically reduce the need for sensor measurements, allowing for simpler, more robust, and less expensive soft root design. Therefore, accurate dynamic forward control of soft roots is an important and still largely unsolved problem.

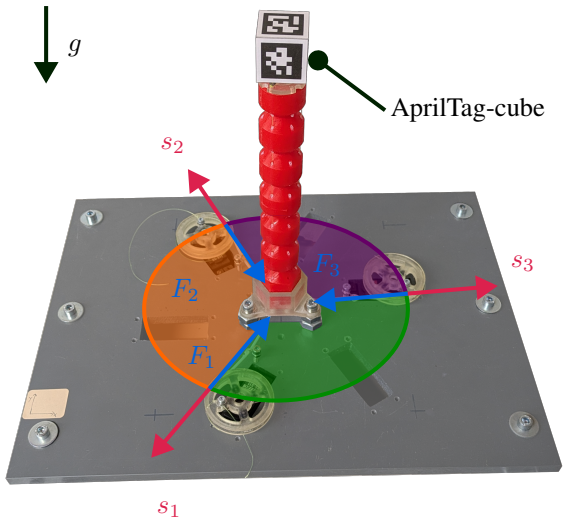

Fig. 1. Soft robot test system: A down-facing camera tracks the Apriltag-cube which is attached to the soft robot (red body). The tendons s_i are guided through holes in the soft body and pulled by the three motors $j = 1 \dots 3$ which are embedded in the ground-platform. The three pieces of the circular disk mark the workspace.

Many works address dynamic forward modeling [5], [6], [7]. However, precise output tracking tasks require known system inputs to reach a desired output. Analytical model inversion is challenging due to its high non-linearity and complexity. Furthermore, soft robots are controlled with a limited amount of actuators and are consequently typically highly underactuated. Thus, not all degrees of freedom can be controlled independently, which further hampers the inversion. Hence, approaches from related fields can be considered. One method is the addition of servo-constraints, a model inversion technique commonly applied to complex underactuated multibody systems [8].

A. Contribution

In this work, we address the inverse dynamics problem by constraining the robot's output to a desired trajectory. We obtain forward dynamics from differentiation of a kinematic model. We invert our model by using servo-constraints and analyze for internal stability. Experimentally, we identify the remaining unknowns of our self-built robot and validate the

[1]Institute of Mechanics and Ocean Engineering, Hamburg University of Technology

[2]Institute of Logistics Engineering, Hamburg University of Technology

strength of this approach by tracking dynamic trajectories with the robot's tip.

II. Soft Robot Test System

Fig. 1 shows the beam-shaped soft robot used in this work. The robot's body is made of "HT45" type silicone in a silicone molding process. It is stiff in the longitudinal direction and allows bending in x- and y-direction. There are six notches along the body for controlled deformation. The soft robot is redundantly actuated by $N_{\text{tendons}} = 3$ tendons running along the outside of the soft robot body. They are placed symmetrically around the circumference. Three servos are used to directly control the length s_j of the tendons $j \in 1 \dots N_{\text{pieces}}$. As system input, we consider the forces $\boldsymbol{u} = \begin{bmatrix} F_1 & F_2 & F_3 \end{bmatrix}^\top$ induced by the tendons. Due to the redundant actuation, only two of the three tendon lengths s_i can be selected independently, otherwise the tendons would become loose or crack. As system output, we track the tip position of the robot $\boldsymbol{z} \in \mathbb{R}^2$. Since $\boldsymbol{u} \in \mathrm{R}^3$, the tip moves on a semi-sphere hull enveloping the robot. For reference measurements, an external camera tracking system based on AprilTags [9] is used. Thus, a cube of size $l_{\text{cube}} = 0.03\,\mathrm{m}$ is attached to the robot's end, where AprilTags of family *36h11* are glued to the sides and top. Tab. I provides a full list of the robot's characteristics.

TABLE I
Characteristics of the soft robot test system.

Dimension	Symbol	Unit	Value
robot length	l_{robot}	m	0.19
robot radius	r_{robot}	m	0.015
length of tendon guide holes	l_{guide}	m	0.014
circle radius of holes	r_{guide}	m	0.0125
motor reel diameter	d_{reel}	m	0.046
end-effector cube mass	m_{cube}	kg	0.017
Mass of silicone body	m_{body}	kg	0.117
Young's modulus	E	MPA	2.04
Shore-hardness (HT 45-silicone)	H	ShA	45
Number of actuation tendonds	N_{tendons}	-	3

III. Forward Model of the Soft Robot

In this section, we draw a kinematic representation for the present robot system and differentiate by time to obtain forward dynamics. We discuss actuation redundancy and introduce system unknowns that influence control.

A. Piecewise Constant Curvature Model

Approaches for modeling soft robot kinematics are commonly based on finite element (FE)-techniques and data-driven models such as the cosserat rod [10], [11] and neural networks, respectively [12], [12]. The piecewise constant curvature (PCC) model is one of the simplest and most intuitive models for beams undergoing large deformations.

1) Discretization: In PCC, a beam is discretized into $i = 1 \dots N_{\text{pieces}}$ pieces of constant curvature using a 1D FE mesh. Each piece consists of a massless elastic link at the end of which a mass-loaded disk is mounted. The stiffness and damping properties are aggregated in the elastic link, and the inertia properties are aggregated in the disk. Bending in two spatial directions, torsion and strain can be modeled with the PCC model. Shear is neglected. The elongation mode is usually very stiff compared to the bending and torsion modes. Therefore, it is often neglected, as in the following. Torsion is also often neglected because in many applications there are no or very small torsional moments . In this work, we explore configurations $N_{\text{pieces}} \in [1, \dots, 6]$.

Each piece has length l_i and mass m_i and is the total value divided by N_{pieces}. Note that for the last piece the mass of the cube m_{cube} is added. The Young modulus E and the second moments of area $I_{\text{loc},xx}$, $I_{\text{loc},yy}$, and $I_{\text{loc},zz}$ oare consistent for all N_{pieces} pieces

$$I_{\text{loc},xx} = I_{\text{loc},yy} = \frac{m_i}{12}(3r_{\text{robot}}^2 + l_i^2), \tag{1}$$

$$I_{\text{loc},zz} = \frac{m_i}{2} r_{\text{robot}}^2. \tag{2}$$

B. Parametrization

There are various parameterizations of the PCC model [13], most of which have problems with removable singularities [14]. We use a parameterization based on [15], which treats singularities, appearing for the straight configuration, with Taylor series expansion.

Two rotations μ_i and ν_i describe the deformation of a piece, as seen in Fig.2. The vector $\boldsymbol{\rho}$ points to the center of rotation

$$\boldsymbol{\rho}_{i,\text{loc}} = \frac{l_i}{\varphi_i^2} \begin{bmatrix} \nu_i & -\mu_i & 0 \end{bmatrix}^\top, \tag{3}$$

where $\varphi_i = \sqrt{\nu_i^2 + \mu_i^2}$ is the total bending angle.

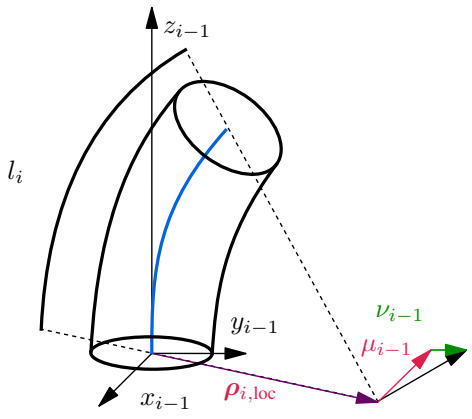

Fig. 2. Parameterization according to [15].

For each piece i, the rotation matrix $\boldsymbol{R}_{i-1,i}$ and position matrix $\boldsymbol{p}_{i,\text{loc}}$ describe the piece's tip (bottom frame of

the adjacent piece) in the current bottom, piece-fixed frame

$$\boldsymbol{p}_{i,\text{loc}} = \begin{bmatrix} -\rho_{i,\text{loc},x}\sigma_i & -\rho_{i,\text{loc},y}\sigma_i & \|\boldsymbol{\rho}_{i,\text{loc}}\|S_{\varphi_i} \end{bmatrix}^\top, \quad (4)$$

$$\boldsymbol{R}_{i-1,i} = \begin{bmatrix} \sigma_i\bar{\nu}_i^2 + 1 & \sigma_i\bar{\mu}_i\bar{\nu}_i & \bar{\nu}_i\sin\varphi_i \\ \sigma_i\bar{\mu}_i\bar{\nu}_i & \sigma_i\bar{\mu}_i^2 + 1 & \bar{\mu}_i\sin\varphi_i \\ -\bar{\nu}_i\sin\varphi_i & -\bar{\mu}_i\sin\varphi_i & \cos\varphi_i \end{bmatrix}, \quad (5)$$

where $\sigma_i = \cos(\varphi_i) - 1$, $\bar{\nu}_i = \dfrac{\nu_i}{\varphi_i}$ and $\bar{\mu}_i = \dfrac{\mu_i}{\varphi_i}$, and $\rho_{i,\text{loc},x}$, and $\rho_{i,\text{loc},y}$ are the x and y entries of $\boldsymbol{\rho}_{i,\text{loc}}$. With the global frame at $\boldsymbol{\rho}_{0,\text{loc}}$, transformation into the global frame of $\boldsymbol{p}_i$ and $\boldsymbol{R}_i$ for each piece is obtained by

$$\boldsymbol{R}_i = \begin{cases} \boldsymbol{R}_{i,\text{loc}} & \text{for} \quad i = 1 \\ \boldsymbol{R}_{i-1} \cdot \boldsymbol{R}_{i-1,i} & \text{for} \quad i > 1 \end{cases}, \quad (6)$$

$$\boldsymbol{p}_i = \begin{cases} \boldsymbol{p}_{i,\text{loc}} & \text{for} \quad i = 1 \\ \boldsymbol{p}_{i-1} + \boldsymbol{R}_{i-1} \cdot \boldsymbol{p}_{i,\text{loc}} & \text{for} \quad i > 1 \end{cases}. \quad (7)$$

C. Internal and External Loads

Internal forces and moments result from its bending stiffness. Although soft robots have typically strong damping, we neglect resulting forces as experiments have shown a damping ratio of only $\delta \approx 0.0032$ for our robot, only considering damping for the stability analysis in IV-B.1. The $x-y$-directional bending can be calculated by modeling the robot as a homogeneous beam [16]. The magnitude of the moment that acts on each piece can be calculated as

$$\boldsymbol{l}_{i,\text{bend}} = EI_{\text{loc},xx} \cdot \frac{\varphi_i]}{l_i}. \quad (8)$$

Considering the free-body diagram of a single elastic piece, both ends experience bending. Therefore, $\boldsymbol{l}_{i,\text{bend}}$ acts on the current piece as well as on the previous piece

$$\boldsymbol{l}_{i,\text{bend}} = -\boldsymbol{l}_{i,\text{bend}} \cdot \boldsymbol{n}_{i,\text{bp}}, \quad (9)$$

$$\boldsymbol{l}_{i+1:i,\text{bend}} = \boldsymbol{l}_{i+1,\text{bend}} \cdot \boldsymbol{n}_{i+1,\text{bp}}. \quad (10)$$

Here $\boldsymbol{n}_{i,\text{bp}}$ is the normal vector of the bending plane

$$\boldsymbol{n}_{i,\text{bp}} = \boldsymbol{R}_{i-1} \cdot \begin{bmatrix} -\sin(\theta_i) & \cos(\theta_i) & 0 \end{bmatrix}^\top, \quad (11)$$

where $\theta_i = \arctan 2(\mu_i, \nu_i)$ is the rotation angle to the bending plane. Note that the combination of the trigonometric functions causes zero division for the robots straight pose, and hence requires Taylor approximations of $\sin$ and $\cos$.

As the robot is positioned upright, the only external force results from gravitation in negative z-direction

$$\boldsymbol{f}_{g,i} = \begin{bmatrix} 0 & 0 & -m_i g \end{bmatrix}^\top. \quad (12)$$

D. Actuation Loads

Actuation of the robot is achieved by three tendons guided through holes in the robots body 3. We neglect tendon friction, which results in constant tendon forces F_j along the three tendons. The position of the holes that guide the tendons are given in the local frame as

$$\boldsymbol{r}^l_{i,j,\text{loc}} = \boldsymbol{R}^z(\phi_j) \begin{bmatrix} r_{\text{guide}} & 0 & -l_{\text{guide}}/2 \end{bmatrix}^\top, \quad (13)$$

$$\boldsymbol{r}^u_{i,j,\text{loc}} = \boldsymbol{R}^z(\phi_j) \begin{bmatrix} r_{\text{guide}} & 0 & l_{\text{guide}}/2 \end{bmatrix}^\top, \quad (14)$$

where $\phi_j \in \{0°, 120°, 240°\}$ for $j = 1 \ldots 3$. Here, r_{guide} is the distance from the piece's center axis to the guide wholes, l_{guide} is the guide's length, and $\boldsymbol{R}^z$ is the rotation matrix around the z-axis. Transformation into the global coordinate frame gives

$$\boldsymbol{r}^q_{i,j} = \boldsymbol{p}_i + \boldsymbol{R}_i \cdot \boldsymbol{r}^q_{i,j,\text{loc}}, \quad (15)$$

for $q \in \{u, l\}$. The forces from the tendons acting on the

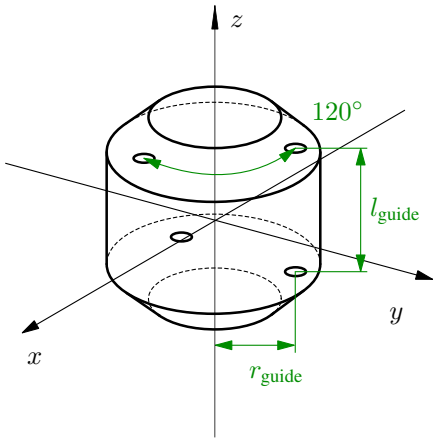

Fig. 3. Positions of the bolt holes that guide the tendons.

pieces of the soft robot can be derived by cutting free the pieces and tendons as shown in Fig. 4. Thereby, it can be assumed without loss of generality that the tendons are fixed in the tendon guides. With the exception of the first and the last piece, each tendon exerts an incoming force $\boldsymbol{f}_{i,i-1,j,\text{tend}}$ and an outgoing force $\boldsymbol{f}_{i,i+1,j,\text{tend}}$ on each piece The magnitude of the forces is equal to the tendon forces F_j, the direction can be derived from the direction of the incoming and outgoing tendon. The effective force directions are obtained by utilizing the positional vectors of two pieces pointing towards adjacent guides. The normalized direction vectors for the forces pointing towards the previous piece are

$$\boldsymbol{c}_{i:i-1,j} = \frac{\boldsymbol{r}^u_{i-1,j} - \boldsymbol{r}^l_{i,j}}{\|\boldsymbol{r}^u_{i-1,j} - \boldsymbol{r}^l_{i,j}\|}, \quad (16)$$

and similar for the adjacent piece

$$\boldsymbol{c}_{i:i+1,j} = \frac{\boldsymbol{r}^l_{i+1,j} - \boldsymbol{r}^u_{i,j}}{\|\boldsymbol{r}^l_{i+1,j} - \boldsymbol{r}^u_{i,j}\|}. \quad (17)$$

Note, for the last piece $i = N_{\text{pieces}}$ $\boldsymbol{c}_{i:i+1,j} = \boldsymbol{0}$. Accordingly, the actuation forces for each piece are given by

$$\boldsymbol{f}_{i:i-1,\text{tendon}} = \sum_{j=1}^{3} \boldsymbol{c}_{i:i-1,j} \cdot F_j, \quad (18)$$

$$\boldsymbol{f}_{i:i+1,\text{tendon}} = \sum_{j=1}^{3} \boldsymbol{c}_{i:i+1,j} \cdot F_j. \quad (19)$$

In addition to the forces, each piece experiences moments as the tendon forces are applied eccentrically. induced by pulling the tendons. Hence, the moments acting on each piece

are

$$\boldsymbol{l}_{i:i-1,\text{tendon}} = \sum_{j=1}^{3} \left(\boldsymbol{R}_i \cdot \boldsymbol{r}^l_{i,j}\right) \times \left(\boldsymbol{c}_{i:i-1,j} \cdot F_j\right), \tag{20}$$

$$\boldsymbol{l}_{i:i+1,\text{tendon}} = \sum_{j=1}^{3} \left(\boldsymbol{R}_i \cdot \boldsymbol{r}^u_{i,j}\right) \times \left(\boldsymbol{c}_{i:i+1,j} \cdot F_j\right). \tag{21}$$

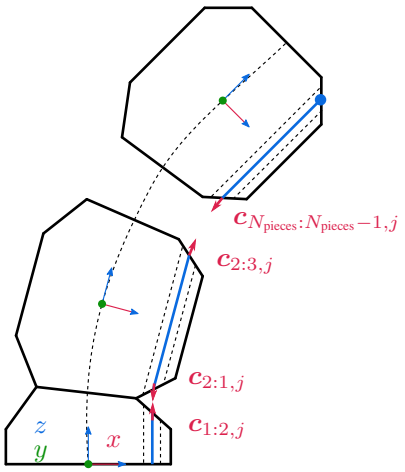

Fig. 4. The acting forces on each piece induced by a tendon's actuation.

1) Modeling tendons: The actuation of the robot is accomplished by pulling the tendons 5. This input is described as a change in length s_j for each tendon j. Further, s_j consists of the geometric change $s_{\text{geo},j}$ and an elastic change $s_{\text{stiff},j}$, due the elongation of each tendon and the robot's own elongation under load

$$s_j = s_{\text{geo},j} + s_{\text{stiff},j}. \tag{22}$$

Considering the robots current state $\boldsymbol{y}$ and the tendon guides relative position in space, the geometric change in length of a single tendon is given by

$$s_{\text{geo},j} = l_{\text{cab},\boldsymbol{y}_0} - \sum_{n=0}^{N} (\|\boldsymbol{r}^l_{n+1,j} - \boldsymbol{r}^u_{n,j}\|)|_{\boldsymbol{y}}. \tag{23}$$

Modeling the elasticity of the tendonds with a virtual spring of stiffness c_j, provides a mapping from force F_j to length s_i. In addition, variations in mounting and pretension of the tendons require consideration, which reasons the introduction of a heuristic deformation coefficient b_j for $s_{\text{geo},j}$.

$$s_j = \frac{F_j}{c_j} + b_j s_{\text{geo},j}. \tag{24}$$

At last, considering the diameter of the reels d_{reel} provides the angular rotation of the motors

$$\alpha_j = \frac{2 s_j}{d_{\text{reel}}}. \tag{25}$$

E. Equations of Motion

With $\boldsymbol{y}_i = \begin{bmatrix}\mu_i & \nu_i\end{bmatrix}^\top$, we define the generalized coordinates $\boldsymbol{y} = \begin{bmatrix}\boldsymbol{y}^\top_{1,\text{loc}} & \cdots & \boldsymbol{y}^\top_{N_{\text{pieces}},\text{loc}}\end{bmatrix}^\top$. The equations of motions are derived following the Newton-Euler formalism, and can be written as second order ordinary differential equations (ODE) in the form

$$\boldsymbol{M}(\boldsymbol{y},t)\ddot{\boldsymbol{y}} + \boldsymbol{k}(\boldsymbol{y},\dot{\boldsymbol{y}},t) = \boldsymbol{q}(\boldsymbol{y},\dot{\boldsymbol{y}},t) + \boldsymbol{B}(\boldsymbol{y})\boldsymbol{u}. \tag{26}$$

With $f = 2N_{\text{pieces}}$, $\boldsymbol{M} \in \mathbb{R}^{f\times f}$ is the mass matrix, $\boldsymbol{k} \in \mathbb{R}^f$ are the Coriolis, centrifugal and gyroscopic forces and $\boldsymbol{q} \in \mathbb{R}^f$ are the applied forces, and $\boldsymbol{B} \in \mathbb{R}^{f\times N_{\text{tendons}}}$ is the input distribution matrix.

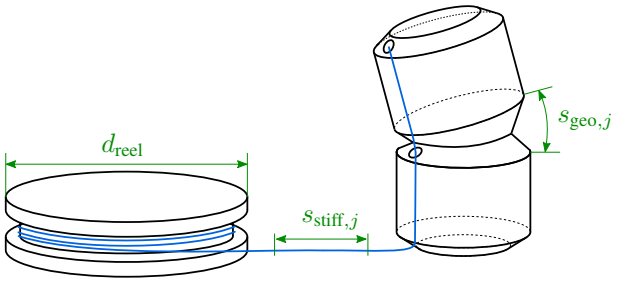

Fig. 5. The motor's rotation causes the robot to bend and tendons to stretch.

IV. Model Inversion using Servo Constraints

For robot control, the inverse of Eq. 26 is needed. We apply the servo-constraints approach [17] to obtain the inverse model, a common approach for underactuated multibody control [18], [19].

A. Inverse Model

To model the system's inverse direction, the equations of motion are extended by additional constraints acting on the system to account for the system's redundancy, and thus eliminate the number of unknowns. Considering the goal of trajectory tracking, constraints on positional level are reasonable. Together with the equations of motion in ODE form Eq. 26, the differential algebraic equations (DAE) are defined as

$$\begin{aligned} \boldsymbol{v} &= \dot{\boldsymbol{y}}, \\ \boldsymbol{M}(\boldsymbol{y},t)\dot{\boldsymbol{v}} &= \boldsymbol{q}(\boldsymbol{y},\boldsymbol{v},t) - \boldsymbol{k}(\boldsymbol{y},\boldsymbol{v},t) + \boldsymbol{B}(\boldsymbol{y})\boldsymbol{u}, \\ \boldsymbol{c}(\boldsymbol{y},t) &= \boldsymbol{h}(\boldsymbol{y}) - \boldsymbol{z}^{\text{des}}(t) = \boldsymbol{0}. \end{aligned} \tag{27}$$

This system is fully described and can be solved for the state vector $\boldsymbol{x} = \begin{bmatrix}\boldsymbol{y}^\top & \boldsymbol{v}^\top & \boldsymbol{u}^\top\end{bmatrix}^\top$. The system's output $\boldsymbol{z} = \boldsymbol{h}(\boldsymbol{y})$ is constrained to be equal to the desired output $\boldsymbol{z}^{\text{des}}(t)$. With the additional constraint, the system is complete.

An output function is defined by considering the semi-sphere hull workspace of the robot. From a top-down view, each point on the hull is defined by considering the $x-$ and $y-$coordinate of the tip position of the robot.

$$\boldsymbol{z} = \boldsymbol{h}(\boldsymbol{y}) = \begin{bmatrix}p_{x,N}(\boldsymbol{y}) & p_{y,N}(\boldsymbol{y})\end{bmatrix}^\top. \tag{28}$$

The robot's stiffness in its longitudinal direction causes a redundant actuation input and an input-mapping is required.

The robot's workspace is divided along the guides into three pieces, as can be seen in Fig. 1. The two forces inside the area of actuation are set as positive, while the remaining force outside of the sub-workspace is set to zero. Additionally, this approach gives the smallest forces in comparison to other approaches, where all forces are higher in general. The workspace distribution is characterized by an angle ψ defined in the x-y plane, giving a mapping

$$\boldsymbol{u} = \boldsymbol{\Phi}^\top \cdot \boldsymbol{u}_{\text{red}}, \tag{29}$$

with $\boldsymbol{u}_{\text{red}}$ denoting the reduced unknown input consisting of the two active forces. The mapping matrix $\boldsymbol{\Phi}$ is dependent on the location of the desired tip position, given by

$$\boldsymbol{\Phi} = \begin{cases} \begin{bmatrix} 1 & 0 & 0 \\ 0 & 1 & 0 \end{bmatrix} & \text{for} \quad \psi \in [0, 120^\circ) \\ \begin{bmatrix} 0 & 1 & 0 \\ 0 & 0 & 1 \end{bmatrix} & \text{for} \quad \psi \in [120^\circ, 240^\circ) \\ \begin{bmatrix} 0 & 0 & 1 \\ 1 & 0 & 0 \end{bmatrix} & \text{for} \quad \psi \in [240^\circ, 360^\circ) \end{cases} \tag{30}$$

with $\psi = \arctan 2(z_y^{\text{des}}, z_x^{\text{des}})$ and z_y^{des} and z_x^{des} being the x and y coordinates of the desired output position of the end-effector.

B. Internal Dynamics and Invertibility Analysis

To guarantee stable control, we analyze the system's internal dynamics and invertibility. We consider the differentiation index, which describes the degree of differentiation of the algebraic system constraints until the DAE can be transformed into ODE form [20]. The input $\boldsymbol{u}$ appears when differentiating $\boldsymbol{c}(\boldsymbol{y}, t)$ twice yielding a differentiation index of 3, which is typical for multi-body systems [21]. Substitution of Eq. ODE for $\dot{\boldsymbol{v}}$ gives the feed-forward control input

$$\widetilde{\boldsymbol{u}}(t) = (\widetilde{\boldsymbol{H}}\widetilde{\boldsymbol{M}}^{-1}\widetilde{\boldsymbol{B}})^{-1}(\ddot{\boldsymbol{z}}^{\text{des}} - \widetilde{\boldsymbol{H}}\widetilde{\boldsymbol{M}}^{-1}(\widetilde{\boldsymbol{q}} - \widetilde{\boldsymbol{k}}) - \widetilde{\boldsymbol{H}}\boldsymbol{v}), \tag{31}$$

where $\boldsymbol{H} = \frac{\partial \boldsymbol{h}}{\partial \boldsymbol{y}}$ and the tilde marks quantities evaluated for $\widetilde{\boldsymbol{x}}$, the state required to reach $\ddot{\boldsymbol{z}}^{\text{des}}$. For full rank of $\mathbf{Y}(\boldsymbol{y}) = \widetilde{\boldsymbol{H}}\widetilde{\boldsymbol{M}}^{-1}\widetilde{\boldsymbol{B}}$, the input $\boldsymbol{u}$ directly influences all system outputs and a control law can be established straightforward [17].

In the following analysis, we only consider the case $N_{\text{pieces}} = 2$, which yields a multi-body configuration while staying computationally cheap when solving Eq. 27 using an implicit Euler approach. As the solver remains stable for $N_{\text{pieces}} \geq 2$, we assume that stability remains for more complex models.

1) Stability Analysis of the Inverse System: Full-specified motion is only given for $N_{\text{pieces}} = 1$ with $N_{\text{tendons}} = \dim(\boldsymbol{z}) = f = 2$. For $N_{\text{pieces}} \geq 2$, internal dynamics may cause destabilization and servo-constraints have to be designed through dynamic couplings in the system instead [17]. A non-linear system is of minimum phase if it has stable zero dynamics [22]. Thus, we linearize the inverse model of Eq. 26 at a stationary point $\boldsymbol{x}_{\text{eq}}$. For small values around the point of equilibrium $\widetilde{\boldsymbol{y}} = \boldsymbol{y} - \boldsymbol{y}_{\text{eq}}$, $\widetilde{\boldsymbol{v}} = \boldsymbol{v} - \boldsymbol{v}_{\text{eq}}$ and $\widetilde{\boldsymbol{u}} = \boldsymbol{u} - \boldsymbol{u}_{\text{eq}}$ are

$$\boldsymbol{M}_{\text{lin}}\dot{\widetilde{\boldsymbol{v}}} + \boldsymbol{D}_{\text{lin}}\widetilde{\boldsymbol{v}} + \boldsymbol{K}_{\text{lin}}\widetilde{\boldsymbol{y}} = \boldsymbol{B}_{\text{lin}}\widetilde{\boldsymbol{u}} \tag{32}$$

$$\boldsymbol{H}_{\text{lin}}\widetilde{\boldsymbol{y}} = \boldsymbol{0}, \tag{33}$$

with $\boldsymbol{M}_{\text{lin}} = \boldsymbol{M}(\boldsymbol{y}_{\text{eq}})$, $\boldsymbol{B}_{\text{lin}} = \boldsymbol{B}(\boldsymbol{y}_{\text{eq}})$, $\boldsymbol{H}_{\text{lin}} = \boldsymbol{H}(\boldsymbol{y}_{\text{eq}})$, and

$$\boldsymbol{D}_{\text{lin}} = \boldsymbol{C} + \left(\frac{\partial \boldsymbol{k}}{\partial \boldsymbol{v}} - \frac{\partial \boldsymbol{q}}{\partial \boldsymbol{v}}\right)\Big|_{\boldsymbol{y}_{\text{eq}}, \boldsymbol{v}_{\text{eq}}}, \tag{34}$$

$$\boldsymbol{K}_{\text{lin}} = \left(\frac{\partial \boldsymbol{k}}{\partial \boldsymbol{y}} - \frac{\partial \boldsymbol{q}}{\partial \boldsymbol{y}} - \frac{\partial \boldsymbol{B}\boldsymbol{u}_{\text{eq}}}{\partial \boldsymbol{y}}\right)\Big|_{\boldsymbol{y}_{\text{eq}}, \dot{\boldsymbol{y}}_{\text{eq}}}. \tag{35}$$

The linearized equations can be rewritten as

$$\boldsymbol{E}^*\dot{\widetilde{\boldsymbol{x}}} = \boldsymbol{A}^*\widetilde{\boldsymbol{x}} \tag{36}$$

with the augmented state vector

$$\widetilde{\boldsymbol{x}} = \begin{bmatrix} \widetilde{\boldsymbol{y}}^\top & \widetilde{\boldsymbol{v}}^\top & \widetilde{\boldsymbol{u}}^\top \end{bmatrix}^\top \tag{37}$$

and the two matrices

$$\boldsymbol{E}^* = \begin{bmatrix} \mathbf{I} & \mathbf{0} & \mathbf{0} \\ \mathbf{0} & \boldsymbol{M}_{\text{lin}} & \mathbf{0} \\ \mathbf{0} & \mathbf{0} & \mathbf{0} \end{bmatrix} \tag{38}$$

$$\boldsymbol{A}^* = \begin{bmatrix} \mathbf{0} & \mathbf{I} & \mathbf{0} \\ -\boldsymbol{K}_{\text{lin}} & -\boldsymbol{D}_{\text{lin}} & \boldsymbol{B}_{\text{lin}} \\ \boldsymbol{H}_{\text{lin}} & \mathbf{0} & \mathbf{0} \end{bmatrix}. \tag{39}$$

Rearranging 36 gives the eigenvalue problem

$$(\boldsymbol{A}^* - \lambda \boldsymbol{E}^*)\mathbf{c}^* = \mathbf{0}. \tag{40}$$

Infinite eigenvalues result from algebraic constraints with infinitely fast motion [23]. Invariant poles $\lambda < \infty$ determine if the system is of minimum phase. As the system is rotationally symmetric, only a single workspace-section is considered. Given a point of equilibrium by evaluating Eq. 26 for $\boldsymbol{v} = \mathbf{0}$ and $\dot{\boldsymbol{v}} = \mathbf{0}$ for an arbitrary force $\boldsymbol{u} = \begin{bmatrix} 1 & 1 & 0 \end{bmatrix}^T$ and solving Eq. 40 for λ shows internal stability of the inverse system, as seen in Fig. 6. All λ are positioned in the left-hand plane confirming minimum-phase.

2) Relative Degree: Continuous differentiability of $\boldsymbol{z}^{\text{des}}$ is required for a control law to exist. For this purpose, the relative degree r_{rel} describes the number of derivatives of $\boldsymbol{z}$ until $\boldsymbol{z}$ appears and serves as the differentiability index of $\boldsymbol{z}^{\text{des}}$ [24]. Differentiating $\boldsymbol{z}$ and substituting 26 for $\boldsymbol{u}$ gives

$$\ddot{\boldsymbol{z}} = \boldsymbol{H}(\boldsymbol{M}^{-1}(\boldsymbol{q} - \boldsymbol{k} + \boldsymbol{B}\boldsymbol{u})) + \dot{\boldsymbol{H}}\boldsymbol{v}. \tag{41}$$

With Eq. 41 being of second order degree and $\mathbf{Y}$ having full rank, the system has $\text{rank}(\mathbf{Y}) = r_{\text{rel}} = 2$. This confirms with the differentiation index being $r_{\text{rel}} + 1$, an ideal configuration for inverse model DAE according to [25], and hence the desired trajectories have to be of second order degree. It is assumed that the r_{rel} is independent of N_{pieces} as proving continuous differentiability for $N_{\text{pieces}} > 2$ remains challenging due to the high complexity.

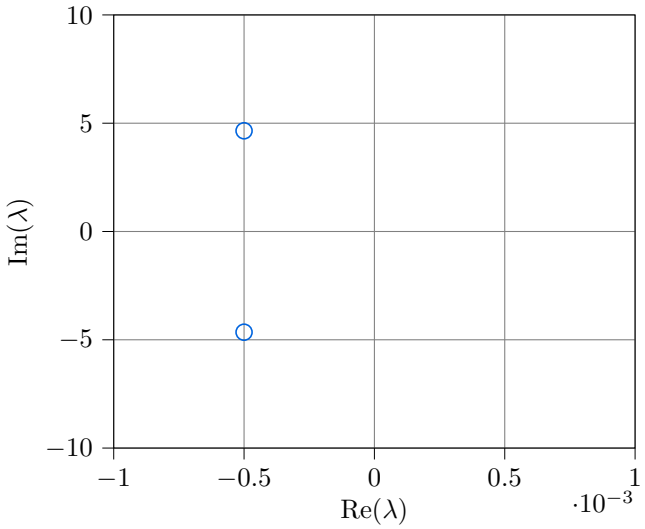

Fig. 6. Eigenvalues of the inverse system.

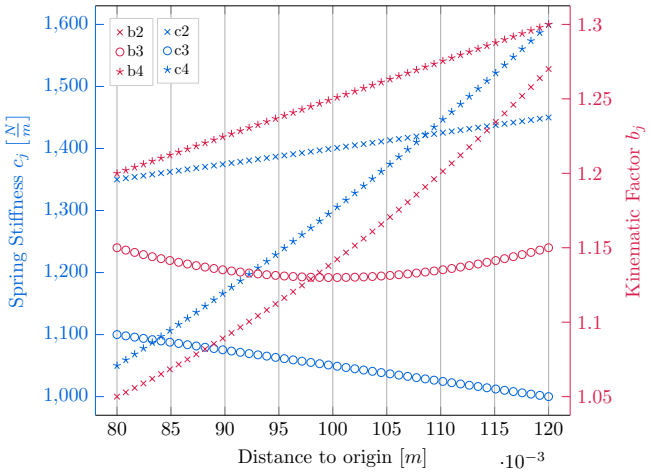

Fig. 7. Polynomials to approximate the coefficients b_j and c_j.

V. Experimental Evaluation

We study the effectiveness of this approach on circular and triangular trajectory. First, we derive function approximators for b_j and c_j. Second, we evaluate the effects of speed and discretization degree N_{pieces} on the positional accuracy.

A. Actuation Coefficients Identification

First, we tune the heuristic deformation and spring stiffness coefficients b_j and c_j. For this purpose, the average positional error of the end-effector in relation to the robot's center is introduced as

$$e_{\text{avg}} = \text{mean}\left(\frac{\|\boldsymbol{z}^{\text{des}}{}_t - \boldsymbol{z}_t^{\text{meas}}\|}{r_c}\right), \tag{42}$$

where $\boldsymbol{z}_t^{\text{meas}}$ and $\boldsymbol{z}^{\text{des}}{}_t$ denote the measured and desired position of the endeffector in the x-y plane, respectively. The coefficients are determined using circular trajectories centered around the robot's base. Consequently, e_{avg} is normalized by the radius r_c of a circle. As during the stability analysis, the DAE in Eq. 27 are solved using implicit Euler with a frequency of $10 \ldots 100\,\text{Hz}$. No significant influence on the robot's performance was found within this range. Early experiments showed that constant b_j and c_j as well as r_c-based linear scaling are insufficient for precise tracking. Thus, we tune coefficients for a handful of circles experimentally and fit polynomial function approximators of second-order degree dependent on the current distance between the robot's tip and center. Note that rather larger radii are sampled as close to the center smaller forces act on the robot body, and friction effects predominate actuation forces, impacting tracking quality. The approximators for $c_j(\|\boldsymbol{z}^{\text{des}}{}_t\|)$ and $b_j(\|\boldsymbol{z}^{\text{des}}{}_t\|)$ are shown in Fig. 7. The parameters are listed in Tab. II.

TABLE II
Polynomial coefficients for representing c_j and b_j.

Coefficient	Unit	Value for $r_c \in \{0.04, 0.08, 0.12\}$cm		
b_1	–	1.05	1.14	1.27
b_2	–	1.15	1.13	1.15
b_3	–	1.2	1.25	1.3
c_1	N/m	1350	1400	1450
c_2	N/m	1100	1050	1000
c_3	N/m	1050	1300	1600

B. Trajectory Tracking

We introduce two distinctive trajectories, which reveal the robot's dynamic nature, a circular path and an equilateral triangle. Circular motion around the robot's base causes centrifugal effects. The triangle provides straight paths and sharp turns, which pose challenges to the actuation. All trajectories are of constant velocity v_{max} with linear acceleration with maximum acceleration $a_{\text{max}} = 0.1\,\frac{\text{m}}{\text{s}^2}$ and jerk $j_{\text{max}} = 0.1\,\frac{\text{m}}{\text{s}^3}$. The robot takes at least one full lap before deaccelerating again. It should be noted that, for certain configurations, the solver struggled to find solutions during the initial deflection, where a slight adjustment of the initial position was sufficient.

1) Circular Trajectory: Three circles of different radii are studied. At $r_c = 4\,\text{cm}$, tracking is significantly affected by friction due to the small actuation forces. In contrast, $r_c = 12\,\text{cm}$ closes the robot's workspace. At last, $r_c = 8\,\text{cm}$ serves as an intermediate.

Tab. III shows the average positional error e_{avg} for varying v_{max} and r_c. In general, the higher the velocity the larger e_{avg}. However, e_{avg} remains relatively even across all r_c at $v_{\text{max}} = 0.05\,\frac{\text{m}}{\text{s}}$, where dynamic inertia and vibration are small. For the small circle $r_c = 0.04\,\text{m}$, disruptive effect of cause tracking inaccuracy resulting in the highest $e_{\text{avg}} = 0.314$, overall. Motion along the workspace limits for $r_c = 0.12\,\text{m}$ is plagued by actuation limits of the motors, causing drift in the end-effectors position. Highest accuracy is achieved at $r_c = 0.08\,\text{m}$, where disruptive effects collectively have the

TABLE III

ERROR e_{AVG} ON TRACKING CIRCLES OF RADII r_c AND VELOCITY v_{MAX}.

Circle size	$v_{\max} = 0.05\ \frac{\text{m}}{\text{s}}$	$v_{\max} = 0.075\ \frac{\text{m}}{\text{s}}$	$v_{\max} = 0.1\ \frac{\text{m}}{\text{s}}$
$r_c = 0.04\,\text{m}$	**0.144**	**0.228**	**0.314**
$r_c = 0.08\,\text{m}$	0.114	0.148	0.209
$r_c = 0.12\,\text{m}$	0.128	0.174	0.25

least impact.

Derivation of dynamics with $N_{\text{pieces}} = 6$ kinematics comes at the cost of enormously higher computation power, which raises the question if a less complex representation impact dynamic tracking quality. Fig. 8 visualizes tracking for $N_{\text{pieces}} \in \{1, 3, 6\}$. A clear decrease in performance is apparent for simpler modeling, where strong deformations can be modeled less accurately.

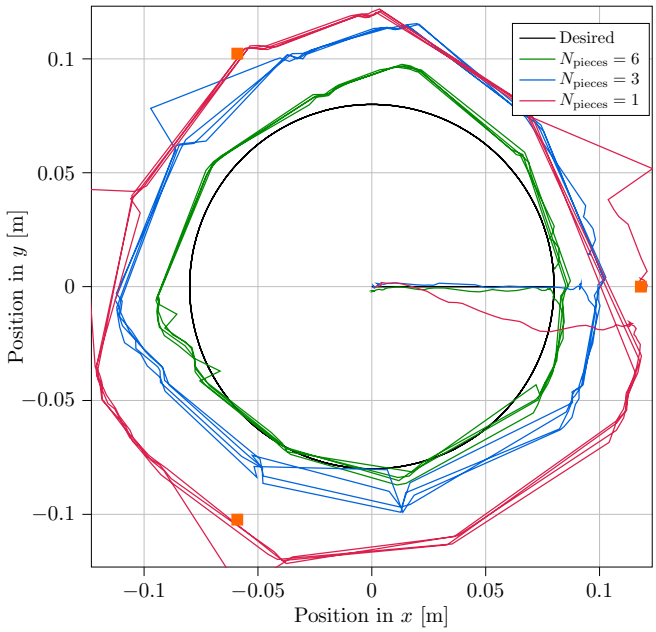

Fig. 8. Tracking a circle of $r_c = 0.08\,\text{m}$ with $v_{\max} = 0.1\ \frac{\text{m}}{\text{s}}$ for varying $N_{\text{pieces}} \in \{1, 3, 6\}$. The orange squares mark the servo-motor locations.

2) Triangular Trajectory: We examine two triangular trajectories, one whose corners align with the actuator positions and another mirrored vertically. Their size is chosen to avoid workspace limits. We set $v_{\max} = 0.1\ \frac{\text{m}}{\text{s}}$ and $N_{\text{pieces}} = 6$.

Fig. 9 compares ground-truth to the measured tip position. In both cases, the robot is capable of tracking the straight lines, where strong deformations occur only closer to the corners. Especially for the aligned path, the sharp turns at the corners is apparent.

3) Interpretation: Overall, the approach demonstrates strong tracking performance for dynamic motions. However, a number of positional offsets are present in all cases, which can be traced back to various reasons. First, the tendons are fixated with strong tape only, which causes loosening over time. Second, variations in assembly and pretension of tendons plagued tuning of b_j and c_j. Hence, repetitive offsets

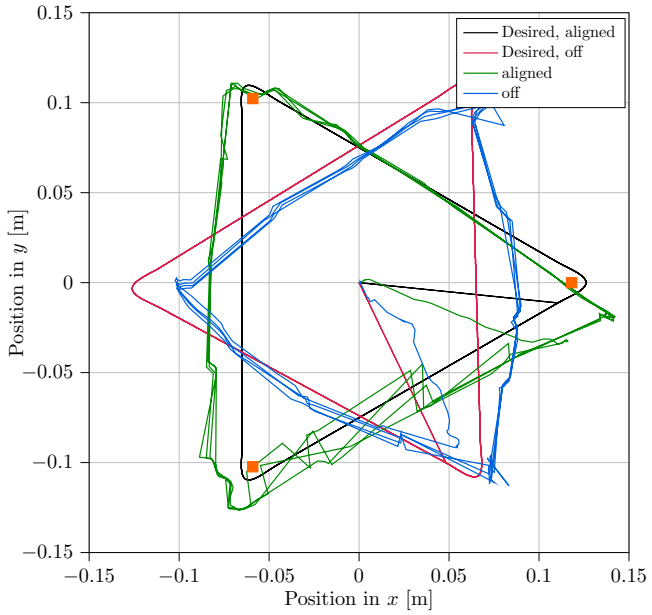

Fig. 9. Tracking equilateral triangles with $v_{\max} = 0.1\ \frac{\text{m}}{\text{s}}$ and $N_{\text{pieces}} = 6$. The orange squares mark the servo-motor locations.

were challenging to avoid as the function approximators scale with $\|\boldsymbol{z}^{\text{des}}{}_t\|$, only. In particular, the triangular paths indicate that the motor at $(0.12, 0)$ suffers from mounting inaccuracies and restricts the robot in reaching the desired far-left and -right corners. Consequently, the robot overshoots at the opposite straight edges.

VI. CONCLUSION

In this work, we presented a model-based feed-forward dynamic control approach for beam-shaped soft robots. Under the assumption of piece-wise constant curvature, we derive forward dynamics and inverse the model applying servo-constraints. We study internal stability of the inverse dynamics and tuned actuation coefficients in a practical manner. We perform experiments on trajectory tracking using a real-world test system to validate the applicability of our approach. The results show limitations in our actuation functions and sensitivity to motor limits, pretension, and mounting variation.

In future work, we aim to improve the system's setup with fixed tendons and constant pretension. Second, we plan to improve the actuation function using learning-based approaches to account for uncertainties. Last, an increase in the number of tendons enables research on dynamic control under more complex deformation.

References are important to the reader; therefore, each citation must be complete and correct. If at all possible, references should be commonly available publications.

REFERENCES

[1] L. Qin, H. Peng, X. Huang, M. Liu, and W. Huang, "Modeling and simulation of dynamics in soft robotics: a review of numerical approaches," *Current Robotics Reports*, vol. 5, no. 1, pp. 1–13, Mar

2024. [Online]. Available: https://doi.org/10.1007/s43154-023-00105-z

[2] R. Webster and B. Jones, "Design and kinematic modeling of constant curvature continuum robots: A review," *I. J. Robotic Res.*, pp. 1661–1683, 2010.

[3] T. Thuruthel, Y. Ansari, E. Falotico, and C. Laschi, "Control strategies for soft robotic manipulators: A survey," *Soft Robotics*, 2018.

[4] C. Della Santina, R. K. Katzschmann, A. Bicchi, and D. Rus, "Model-based dynamic feedback control of a planar soft robot: trajectory tracking and interaction with the environment," *The International Journal of Robotics Research*, 2020.

[5] S. W. Jensen, C. C. Johnson, A. M. Lindberg, and M. D. Killpack, "Tractable and intuitive dynamic model for soft robots via the recursive newton-euler algorithm," in *2022 IEEE 5th International Conference on Soft Robotics*, 2022, pp. 416–422.

[6] A. Amouri, C. Mahfoudi, and A. Zaatri, "Dynamic modeling of a spatial cable-driven continuum robot using euler-lagrange method," 2019.

[7] T. Thuruthel, F. Renda, and F. Iida, "First-order dynamic modeling and control of soft robots," *Frontiers in Robotics and AI*, vol. 7, 2020.

[8] V. Kirgetov, "The motion of controlled mechanical systems with prescribed constraints (servoconstraints)," *Journal of Applied Mathematics and Mechanics*, pp. 465–477, 1967.

[9] E. Olson, "Apriltag: A robust and flexible visual fiducial system," 2011, pp. 3400 – 3407.

[10] M. Giorelli, F. Renda, M. Calisti, A. Arienti, G. Ferri, and C. Laschi, "Learning the inverse kinetics of an octopus-like manipulator in three-dimensional space," *Bioinspiration & biomimetics*, 2015.

[11] F. Renda, M. Giorelli, M. Calisti, M. Cianchetti, and C. Laschi, "Dynamic model of a multibending soft robot arm driven by cables," *IEEE Transactions on Robotics*, pp. 1109–1122, 2014.

[12] Z. Jiang, D. Shah, H.-J. Yang, and S. Sarkar, "Data-driven kinematic modeling in soft robots: System identification and uncertainty quantification," 2025. [Online]. Available: https://arxiv.org/abs/2507.07370

[13] R. J. WebsterIII and B. A. Jones, "Design and kinematic modeling of constant curvature continuum robots: A review," *The International Journal of Robotics Research*, vol. 29, no. 13, pp. 1661–1683, 2010.

[14] C. Della Santina, A. Bicchi, and D. Rus, "On an improved state parametrization for soft robots with piecewise constant curvature and its use in model based control," *IEEE Robotics and Automation Letters*, vol. 5, no. 2, pp. 1001–1008, 2020.

[15] T. F. Allen, L. Rupert, T. R. Duggan, G. Hein, and K. Albert, "Closed-form non-singular constant-curvature continuum manipulator kinematics," in *2020 3rd IEEE International Conference on Soft Robotics (RoboSoft)*, 2020, pp. 410–416.

[16] D. Gross, W. Hauger, J. Schröder, and W. A. Wall, *Technische Mechanik 2: Band 2: Elastostatik (Springer-Lehrbuch)*. Springer, Berlin, 2009.

[17] W. Blajer, R. Seifried, and K. Kolodziejczyk, "Servo-constraint realization for underactuated mechanical systems," *Archive of Applied Mechanics*, 2015.

[18] S. Drücker and R. Seifried, "Real-time trajectory control of an overhead crane using servo-constraints," *Multibody System Dynamics*, vol. 42, 01 2018.

[19] R. Seifried and M. Burkhardt, "Servo-constraints for control of flexible multibody systems with contact," vol. 7, 08 2013.

[20] E. Hairer and G. Wanner, *Solving Ordinary Differential Equations II. Stiff and Differential-Algebraic Problems*, 01 1996, vol. 14.

[21] R. Seifried and W. Blajer, "Analysis of servo-constraint problems for underactuated multibody systems," *Mechanical Sciences*, vol. 4, no. 1, pp. 113–129, 2013. [Online]. Available: https://ms.copernicus.org/articles/4/113/2013/

[22] R. Seifried, *Dynamics of Underactuated Multibody Systems: Modeling, Control and Optimal Design*, 2014.

[23] M. Géradin and A. Cardona, *Flexible Multibody Dynamics: A Finite Element Approach*, 2001.

[24] A. Isidori, *Nonlinear Control Systems: An Introduction*. Berlin, Heidelberg: Springer-Verlag, 1986.

[25] S. L. Campbell, "High-index differential algebraic equations," *Mechanics of Structures and Machines*, vol. 23, no. 2, pp. 199–222, 1995. [Online]. Available: https://doi.org/10.1080/08905459508905235